Received: 5 October 2022 | Accepted: 30 December 2022

DOI: 10.1002/nano.202200212

RESEARCH ARTICLE

Nano Select WILEY

Design of micro- and macro-scale polymeric metamaterial solutions for passive and active thermal camouflaging applications

Harshil Pisavadia[1] | **Asad Asad**[1] | **Dan Sameoto**[1] | **Patricia Dolez**[2] | **James D. Hogan**[1]

[1]Department of Mechanical Engineering, University of Alberta, Edmonton, Canada

[2]Department of Human Ecology, University of Alberta, Edmonton, Canada

Correspondence
Harshil Pisavadia, Department of Mechanical Engineering, University of Alberta, Edmonton, AB T6G 2R3, Canada.
Email: pisavadi@ualberta.ca

Funding information
Department of National Defence of Canada, Grant/Award Number: W7714-228051/001/SV1.herein

Abstract

This work utilizes predictive modeling techniques to guide and inform metamaterial design for heat management solutions and thermal radiation control. Specifically, micro- and macro-scale polyethylene-based solutions are proposed for passive and active thermal camouflage. A micro-scale post design is proposed for highly-tunable infrared emissivity based on varying unit cell geometrical configurations. Actively modulating these micro-features through lateral straining of up to 3% allows for redshifting the emissivity spectrum by up to 0.5 μm. Macro-scale lenticular lens designs allow for a more passive form of camouflage due to its emissive stability for a range of configurations (e.g., single and sandwiched structures, increasing lens radii and height). Overall, the proposed metamaterial designs allow the tailoring of optical properties to improve thermal radiating performance.

KEYWORDS

infrared emissivity, infrared technology, multifunctional metamaterials, multiphysics modeling, thermal camouflage

1 | INTRODUCTION

Tunable mid-infrared (MIR) emitting surfaces and improved infrared (IR) camouflage solutions is an area of high interest by militaries around the world due to hyperspectral imaging technologies being more available. Tunable MIR emissivity in adaptive artificial optical materials is an important metric for various applications including heat management or radiative cooling,[1,2] thermal emitters,[3] thermophotovoltaic cells,[4] infrared communication,[5] and thermal camouflage.[6,7] Metamaterials allow for flexibility in tuning the surface emissivity, which can be achieved by various modulation methods including phase changes,[8,9] altering crystal orientation angles,[6] and electric modulation.[10] However, the majority of this work is conducted experimentally.[11–14] To date, limited studies have applied predictive modeling techniques to inform design decisions for IR management surfaces.[15–17] This article develops predictive modeling capabilities to inform metamaterial structural designs for active and passive thermal signature management solutions.

The two main approaches to achieve and realize IR camouflage are to (1) decrease the surface temperature by reducing thermal radiation through insulation[18–20] and (2) control and tune the surface emissivity spectrum.[6,8,21,22] Metamaterials have been extensively used for thermal camouflaging applications as they can manipulate the optical properties of materials (e.g., reflectivity, transmissivity, and emissivity) through varying their geometrical and optical material parameters.[6,15,21,23–26] For example, Lee et al.[27] developed a metal-dielectric-metal metamaterial to tune the emissivity towards favorable bands (i.e., wavelengths within the non-atmospheric window of 5–8 μm) for radiative cooling applications for aircraft which would otherwise be easily viewed in the atmosphere. In another study, Dang and Ye[15] proposed utilizing photonic crystalline structures to realize (1) heat dissipation by increasing the emittance in the hidden bands within the non-atmospheric window and (2) thermal camouflage by decreasing emissivity within the atmospheric window (wavelengths from 3 μm to 5 μm and 8 μm to 14 μm).

In the literature, the majority of geometrical scales for metamaterial-based IR camouflaging technologies are within the micro-scale regime (< 50 μm) to tune emissivity through resonance and reflectivity[21] and phase transitions.[28] For example, micro-features in the form of cylindrical disk configurations are predominantly used as IR emissive tunable surfaces.[8,9,17] One challenge regarding these micro-scale structures is their manufacturing[7] which requires a multi-step fabrication process that may cause premature deterioration.[29] Increasing the geometric length-scale to the macro-scale (>100 μm) could reduce the complexity and enhance the scalability of these manufacturing processes. To date, no studies have utilized lenticular lenses (experimentally or numerically) to promote optical scattering over Mie scattering for IR camouflage.

Building on past works, the focus of this study is to develop predictive models using COMSOL Multiphysics[30] to inform design decisions when manufacturing polyethylene (PE)-based micro- and macro-scale metamaterials for passive and active thermal camouflaging applications within the MIR wavelength (5–16 μm). PE is the polymer of choice for this study due to its low emissive properties,[29,31,32] ability to be woven into fibers for smart textile applications,[33] elastic durability,[34] and high IR transparency.[35] For the first time in the literature: (1) PE-based patterned metamaterials (specifically, micro- and macro-scale designs) for passive and active thermal management solutions are proposed, (2) a lenticular lens macro-scale design in various configurations (e.g., single-layered and multi-layered systems) is explored for efficient thermal management, (3) active solutions to thermal radiation control are introduced where elastic properties of PE are used to dynamically change the geometrical aspect ratio of the unit cells of metamaterials, and (4) preferable configurations for micro-scale post design (post height, width, and spacing) are proposed. The results are discussed in the context of manufacturing metamaterials for thermal radiation control. Overall, we seek to tailor optical properties (e.g., emissivity and scattering) by designing micro- and macro-scale surface features in PE metamaterials toward our goal of informing more efficient thermal camouflage designs.

2 | RESULTS AND DISCUSSION

In this study, the Electromagnetic Waves Frequency Domain interface within the radio frequency (RF) module in COMSOL Multiphysics is used to simulate the interaction between IR light and three-dimensional (3D) micro- and macro-scale geometries. In particular, Fresnel equations are used to evaluate absorptivity, emissivity, reflectivity, and transmissivity through scattering parameters (S-parameters).[36]

Emissivity (E) and absorbance (A) properties of materials are dependent on their reflectivity (R) and transmissivity (T) through Kirchhoff's law of thermal radiation ($E = A = 1–R–T$).[37] These reflectivity and transmissivity values are dependent on geometrical features and optical properties.[27,28,38] Furthermore, the thermal radiation (P) of a material is dependent on its emissivity through the Stefan Boltzmann law ($P = E\sigma T^4$) where σ is the Stefan-Boltzmann constant and T (K) is the surface temperature. Therefore, the above relationship allows the optical properties to be used as performance indicators of IR camouflage. Controlling the geometrical features of metamaterials can shift and tune emissivity values to improve their radiative thermoregulating performance.

This section starts by discussing the validation of the polyethylene material model. Next, three polyethylene-based metamaterial configurations are explored for passive and active thermal camouflaging applications: (1) macro-scale single-layered lenticular lens design, (2) macro-scale sandwiched lenticular lens design, and (3) micro-scale post design.

2.1 | Polyethylene material model validation

This section discusses the validation of the PE material model, as shown in Figure 1. Experimental data of a plain unstructured 10 μm PE sheet from Chen et al.[35] is used to validate the material model. Figure 1A shows a schematic

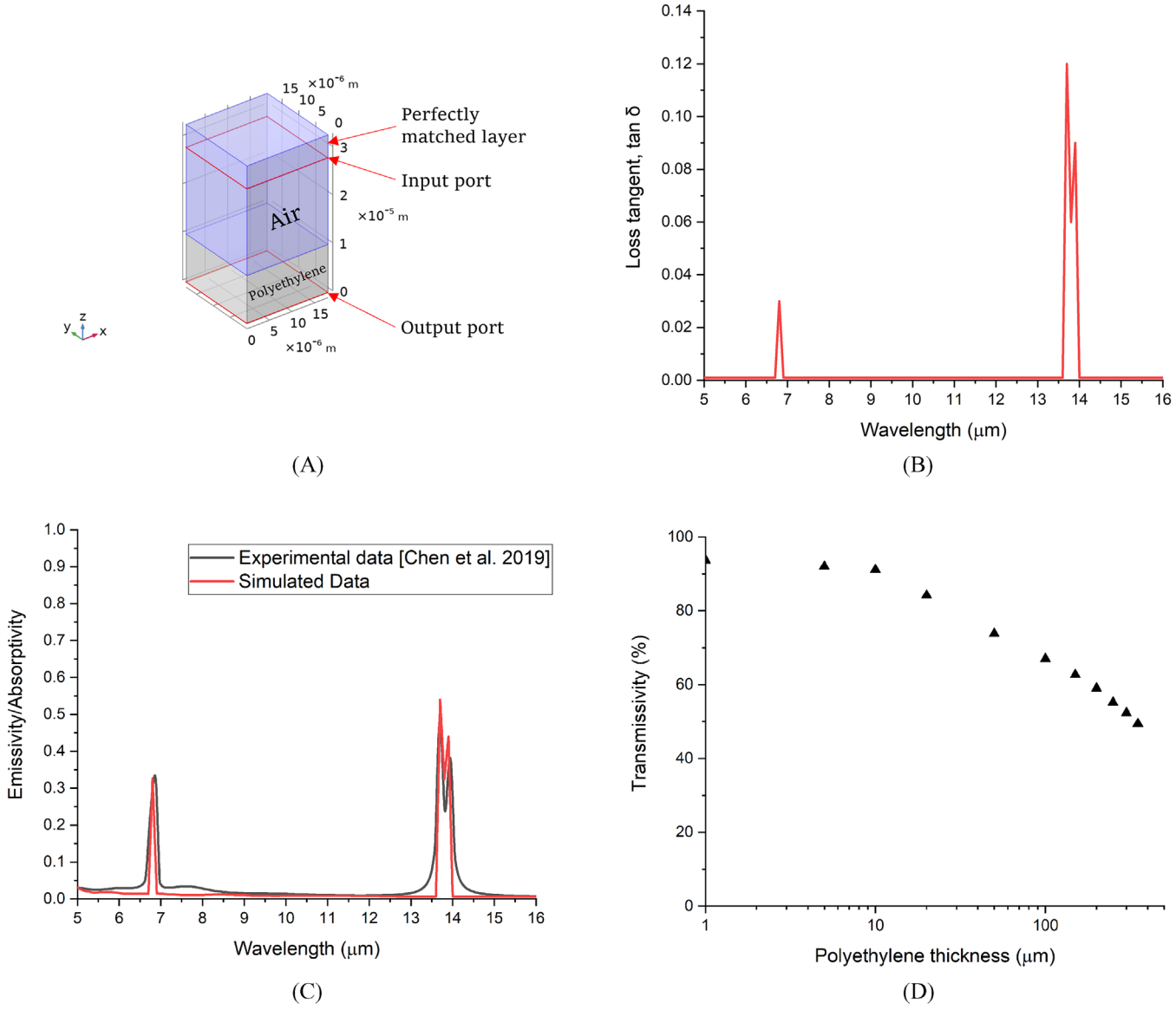

FIGURE 1 COMSOL Multiphysics model validation of a plain unstructured polyethylene sheet. A, Unit cell geometry of a plain 10 μm thick polyethylene sheet with corresponding locations of boundary conditions. Additional Floquet periodic boundary conditions are used in the x- and y-directions. B, Loss tangent-wavelength input plot to COMSOL Multiphysics for a plain 10 μm thick polyethylene sheet. C, Validated emissivity output for a 10 μm thick polyethylene film for the infrared spectrum (wavelengths of 5–16 μm). D, Sensitivity of transmissivity results to polyethylene thickness, where the overall transmissivity decreases with increasing thickness in the infrared spectrum (wavelengths of 5–16 μm)

of a unit cell geometry consisting of a plain 10 μm thick PE sheet exposed to air. Here, the IR rays are orthogonal to the sheet via the input port. The input port also measures the reflected waves from the interaction. Transmissivity is calculated via the output port at the bottom of the PE sheet. In our simulations, the micro-sized features (e.g., lens, posts, sandwich structures) are modeled as unit cells with Floquet periodic boundary conditions in the x- and y-directions. In addition, perfectly matched layers (PMLs) are used above the homogeneous medium (air) along the propagation direction to absorb reflected and radiated waves while minimizing surface reflections. This setup is similar to others in the literature.[15,39,40]

In this study, the PE material model is simulated using the loss tangent dissipation factor electric displacement field model. Shown in Figure 1B is the loss-tangent to wavelength input. Here, the loss tangent is not constant and is instead dependent on the wavelength and frequency of light[41] where peaks are observed in the infrared regime due to ionic mechanisms of the material.[42] In the case of PE-based polymers within the IR regime, these peaks result from the carbon–hydrogen (C–H) and

carbon–carbon (C–C) bonds. Our model informs the loss tangent values for the MIR spectrum which is in turn used to validate the emittance spectrum.

Comparisons between the experimentally obtained emissivity/absorptivity curves from Chen et al.[35] and simulated results for a plain 10 μm thick PE sheet are presented in Figure 1C. Both the experimental and simulated curves are in close agreement, and therefore, the PE material model is considered validated. Additional work in the literature supports a similar validation procedure.[43,44] Furthermore, a unit cell width sensitivity study was conducted (by varying cell widths from 10 μm to 50 μm), where the magnitudes and locations of peaks within the emissivity spectrum were not found to be sensitive to the specified length scales.

Finally, the sensitivity of transmittance to PE thicknesses (between 1 μm and 350 μm) is presented in Figure 1D in a semi-log plot. Each data point represents the area under the transmissivity curve to evaluate its transparency for each specific sheet thickness. As expected, thinner sheets have a greater overall transmissivity suggesting greater transparency than thicker sheets. Overall, the transmissivity decreases as the PE sheet thickness increases. Therefore, the validated material model can now be used for a wide range of PE sheet thicknesses (from 1 μm to 350 μm), thus being suitable for both micro- and macro-scale based design for thermal radiation control.[38,45]

2.2 | Macro-scale single-layered lenticular lens design

This sub-section explores macro-scale single-layered lenticular lens designs for improving radiative thermoregulating performance, as shown in Figure 2. Figure 2A shows the global overall lens geometry where the inset image shows a unit cell of the lens structure. Here, P is the width of the unit cell, t_p is the base sheet thickness, r is the lens radius, and h is the lens height. Figure 2B shows the resulting emissivity/absorptivity curve within the MIR spectrum for increasing radii from $r = 100$ μm to 750 μm and corresponding lens height from $h = 78$ μm to 6 μm. These configurations are selected from our experience in manufacturing these structures and their optical scattering properties, noting that none of these have been considered before in the literature. A gradual increase in the overall emissivity for increasing wavelengths is seen across all the radii. This suggests that these structures result in emissive stability across all configurations chosen here, which, again, is motivated by our ability to manufacture these structures. Shown in Figure 2C is the resulting optical properties (emissivity/absorptivity and reflectivity) for varying angle of incidence ($\theta = 0°$ to 60°) where a shift in the optical properties is observed. This behavior suggests high dispersion and scatter of MIR waves from their interaction with the lens structures, which has been observed to be favorable for cloaking applications.[46,47] Finally, the contour plot in Figure 2D shows effect of applying a lateral strain ($\varepsilon = 0$ to 0.03) to the lenticular unit cell on resulting shifts in wavelength (x-axis); the single lenticular unit cell with the direction of strain is depicted in the inset. Previous manufacturing studies have used strain actuation for IR emissivity tuning with favorable results,[11,12] and this motivates our computational exploration here. In Figure 2D, applying lateral strains of up to the linear strain limit of PE of $\varepsilon = 0.03$[34] does not have a significant effect on the emissivity of the structure (due to the geometrical scale being larger than the MIR wavelength range), further suggesting a stable emissive configuration is achieved with lenticular lens structures, and this is desirable for passive forms of thermal management.

2.3 | Macro-scale sandwiched lenticular lens design

This sub-section explores the macro-scale lenticular lens design within a sandwiched configuration with orthogonally oriented lenses, as presented in Figure 3. Figure 3A shows the overall geometry of the sandwiched structure (lens facing inwards) considered here, where the inset image shows a unit cell of the configuration. Here, t_{air} is the air gap between the two base sheets of the lenses. A lens facing outwards configuration is also explored under the same orthogonally oriented lenses configuration. Shown in Figure 3B,C is the emissivity plotted against the MIR wavelength for increasing air gaps ($t_{air} = 85$ to 175 μm) and lens radii ($r = 100$ to 750 μm) for both the lens facing inwards and outwards configurations. Similar trends to the single lenticular lens design are observed where the emissivity gradually increases for increasing wavelengths for all radii and air gaps. The lens facing inwards configuration, however, exhibits greater emissivity throughout the entire MIR spectrum for all air gaps and lens radii. Other studies, however, found smoother surfaces exhibit lower emissivity values than with rough surfaces.[48,49] Furthermore, emissive stability within each of the configurations for all radii and air gaps is seen. Finally, Figure 3D shows the resulting optical properties (emissivity/absorptivity and reflectivity) for varying angle of incidence ($\theta = 0°$ to 60°) for the lens facing outwards configuration. The shift in optical properties from varying the angle of incidence suggests high optical scattering resulting from the interaction.

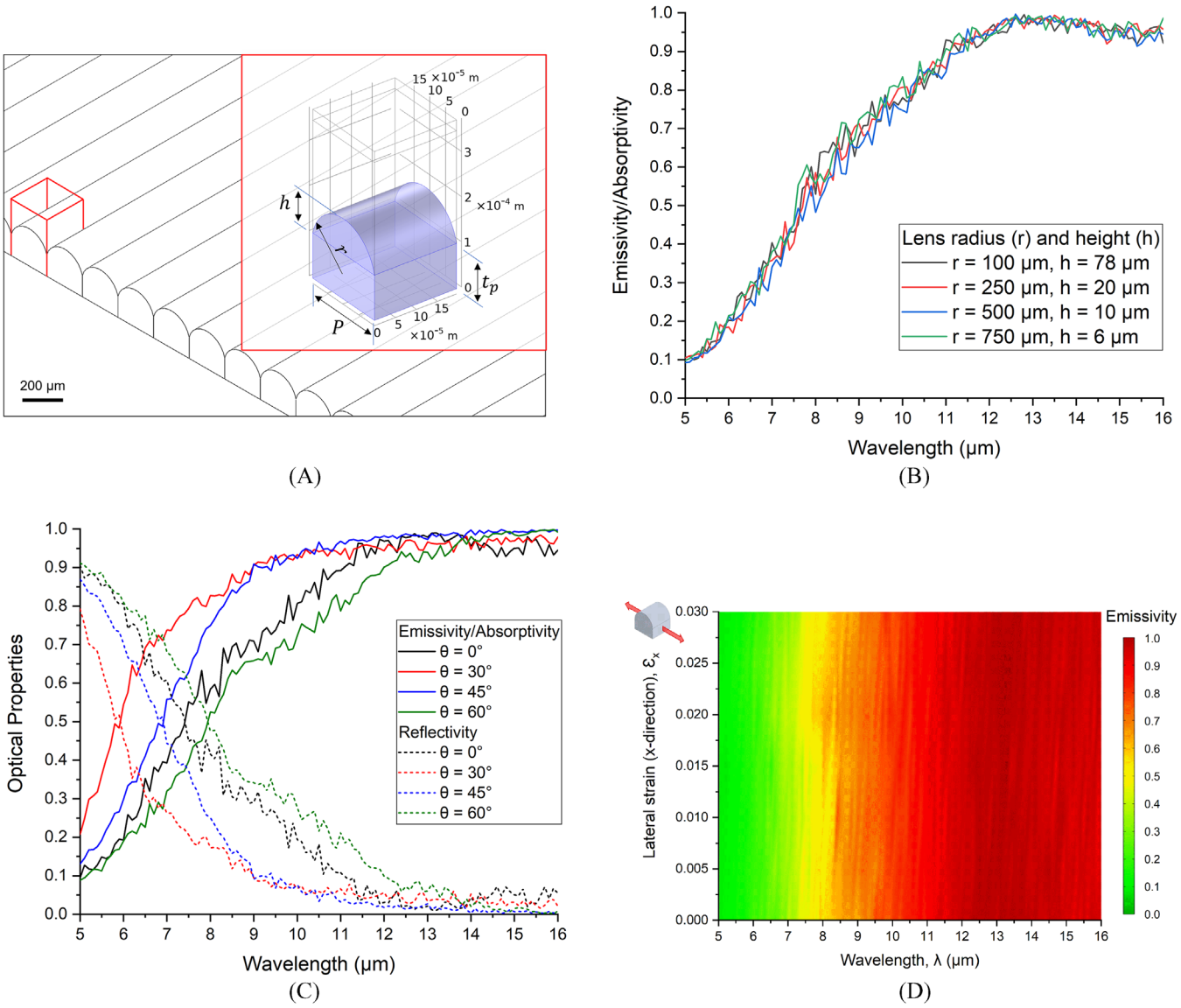

FIGURE 2 Simulating the macro-scale lenticular lens design in COMSOL Multiphysics. A, Global overall lenticular lens geometry. The inset image shows a unit cell geometry where $P = 195$ μm, $r = 100$ to 750 μm, $h = 78$ to 6 μm, and $t_p = 100$ μm. B, Emissivity spectrum of the lenticular lens design with change of lens radius ($r = 100$ to 750 μm and $h = 78$ to 6 μm). C, Emissivity/absorptivity and reflectivity spectra of the lenticular lens design ($r = 150$ μm and $h = 78$ μm) for varying angles of incidence ($\theta = 0°$ to 60°) suggesting a high dispersion of rays. D, Spectral emissivity of the lenticular lens design ($r = 150$ μm and $h = 78$ μm) with an applied lateral strain in the x-direction ($\varepsilon_x = 0$ to 0.03). The inset image shows representative radii of the unit cell with applied lateral strain in the x-direction (not to scale). The macro-scale lenticular lens design allows for a high dispersion of rays while being stable under varying lens radii and strains

2.4 | Micro-scale post design

In this final sub-section, a micro-scale post design is simulated as shown in Figure 4. The overall geometry is presented in Figure 4A with the unit cell configuration shown in the inset image. Here, a is the post width, h is the post height, b is the post spacing, and t_p is the base sheet thickness. Figure 4B shows the emissivity spectrum for various configurations of the post design ($a = h = 1$, 5, and 9 μm, and $b = 1$, 5, and 9 μm), motivated by similar sized disk configurations in the literature.[15,38] Within these configurations, three bands exist which are governed by the post width and height. The smallest post width ($a = 1$ μm) has a similar emissivity spectrum to a plain PE sheet (Figure 1C) where peaks exist due to the ionic mechanisms in the material.[42] This response is comparable to what our team has observed experimentally and is attributed to the geometrical scale of the micro-features and spacings being outside of the MIR wavelength range. Other studies found increasing disk sizes result in a blueshift of emissivity,[17,27] whereas in our study, increasing the post width increases overall emissivity in

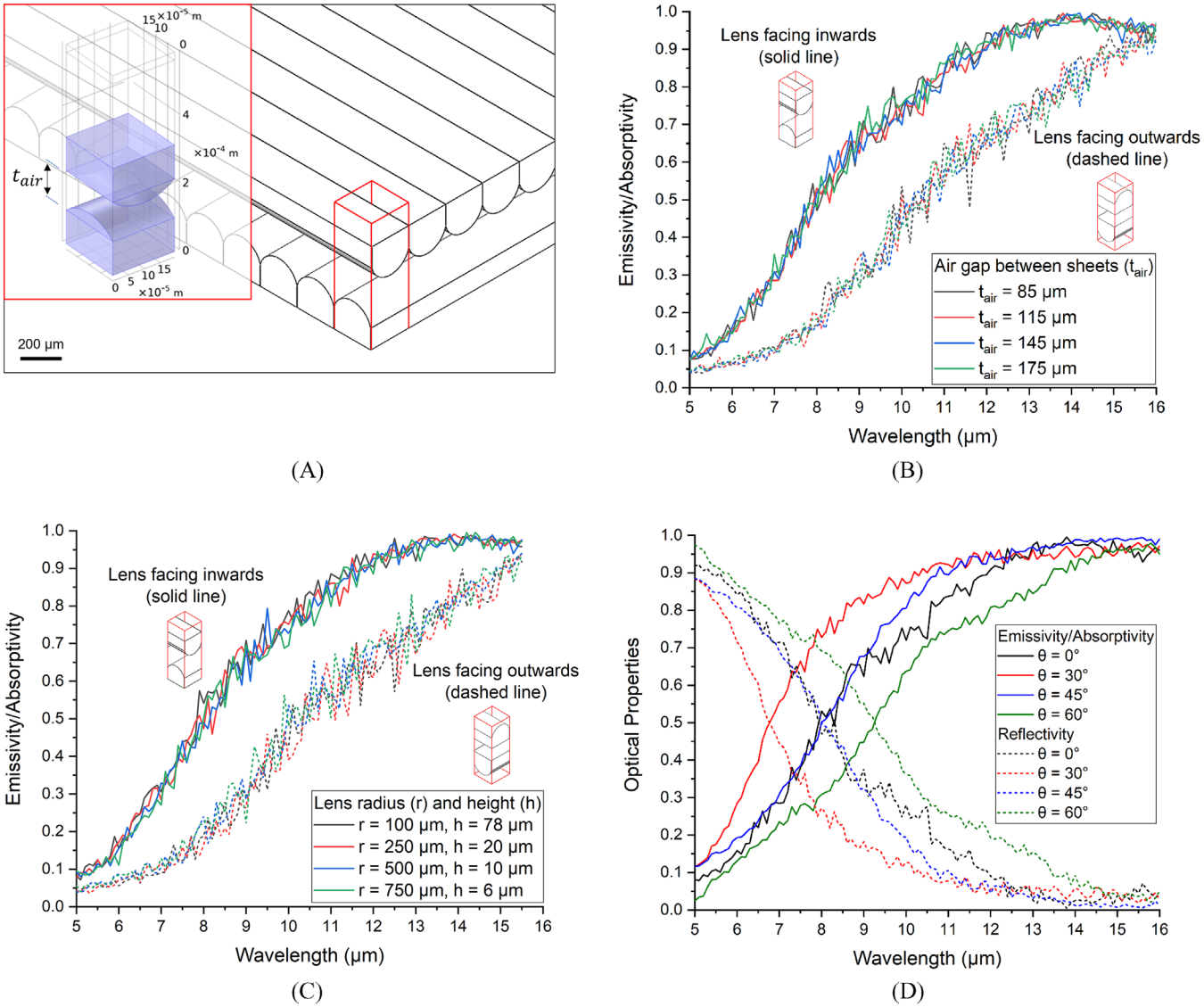

FIGURE 3 Simulating the macro-scale lenticular lens sandwiched structure design in COMSOL Multiphysics. A, Global overall sandwiched lenticular lens geometry (lens facing inwards) with air between the sheets. The inset image shows a unit cell geometry where t_{air} = 85 to 175 μm, r = 100 to 750 μm, h = 78 to 6 μm, and t_p = 100 μm. The configuration with the lens facing outwards is also investigated. Emissivity spectrum of the lenticular lens sandwiched structure with change of: (B) air gap between the lenticular lens sheets (t_{air} = 85 to 175 μm); and (C) change of lens radius (r = 100 to 750 μm and h = 78 to 6 μm) for both lens facing inwards and outwards configurations. The lens facing outwards design has a lower emissivity within the mid-infrared (MIR) wavelengths for all lens radii and air gaps. D, Emissivity/absorptivity and reflectivity spectra of the lenticular lens sandwiched structure (lens facing inwards, r = 150 μm and h = 78 μm) for varying angles of incidence ($\theta = 0°$ to 60°). Similar trends are observed for the lens facing outwards configuration. A high dispersion of rays is evident from the shift of optical properties due to varying angles of incidence of the IR light, while demonstrating emissive stability under the various geometrical configurations

a non-linear manner. Furthermore, emissivity peaks are generated with greater post spacings. The optical properties (emissivity/absorptivity and reflectivity) for varying angles of incidence ($\theta = 0°$ to 60°) for the a = 9 μm and b = 5 μm configuration are plotted in Figure 4C, where this configuration is chosen because a high emissive response is observed within the hidden non-atmospheric band (i.e., wavelengths from 5 μm to 8 μm). The variation in peaks due to the incident angle suggests high dispersion and scatter of rays. Finally, the strain configurations for the unit cell of the posts for up to $\varepsilon = 0.03$ are shown in Figure 4D for the a = 9 μm and b = 5 μm configuration where emissivity is found to redshift by values of up to 0.5 μm. It should be noted that applying strains to the micro-scale post design redshift emissivity to a much greater degree than the macro-scale lenticular lens design, although the manifestation of these shifts for performance needs to be evaluated.

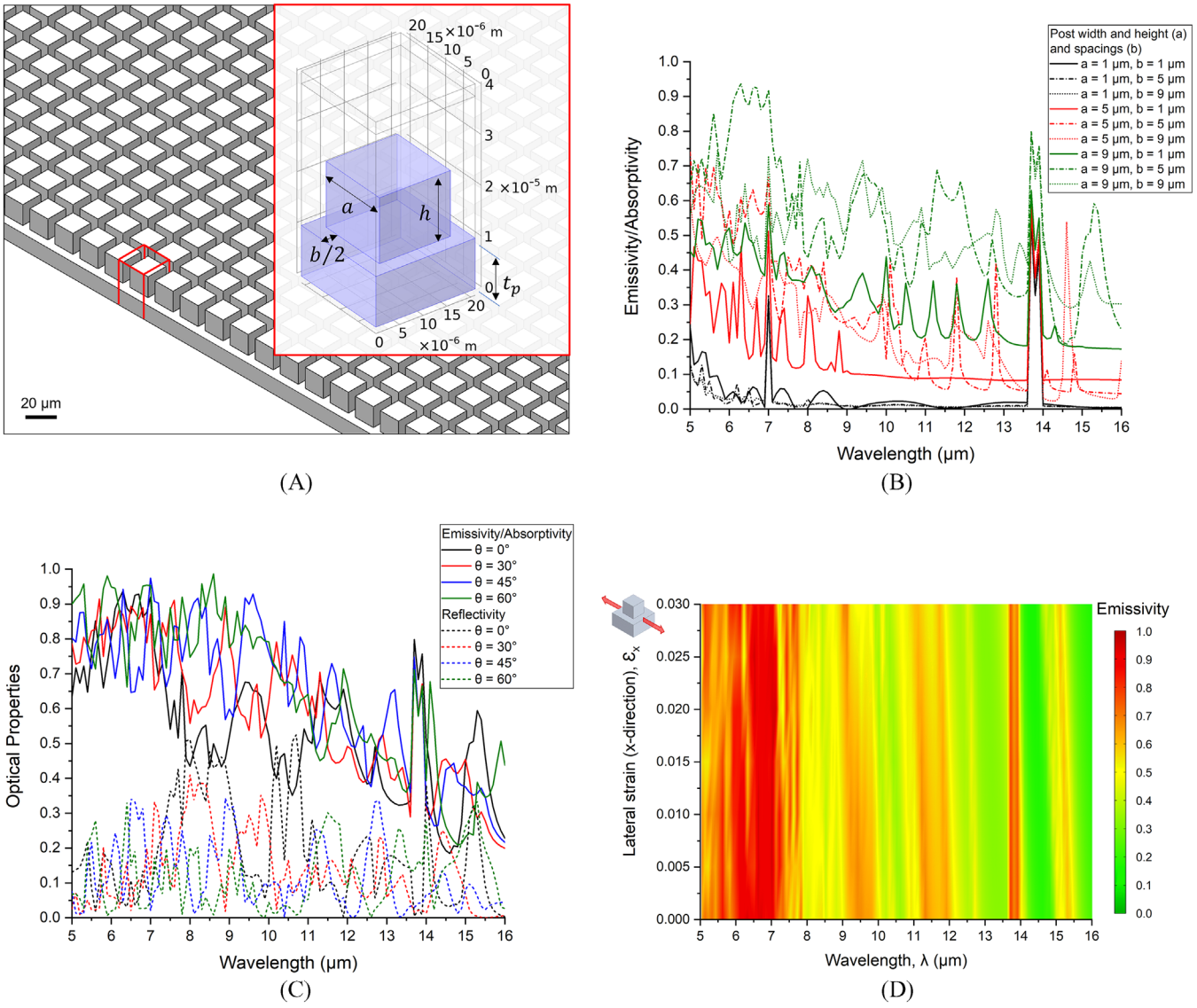

FIGURE 4 Simulating the micro-scale posts design in COMSOL Multiphysics. A, Global overall post geometry. The inset image shows a unit cell geometry where $a = 1$ to 9 μm, $b = 1$ to 9 μm, $h = 1$ to 9 μm, and $t_p = 10$ μm. B, Emissivity spectrum of the post lens design with change in post size and spacing where $a = 1$ to 9 μm, $b = 1$ to 9 μm, and $h = 1$ to 9 μm. C, Emissivity/absorptivity and reflectivity spectra of the post configuration ($a = 9$ μm and $b = 5$ μm) for varying angles of incidence ($\theta = 0°$ to 60°). D, Spectral emissivity of the post configuration ($a = 9$ μm and $b = 5$ μm) with an applied lateral strain in the x-direction ($\varepsilon_x = 0$ to 0.03). Micro-sized posts allow for highly-customizable solutions for thermal radiation control

3 | CONCLUSION

In summary, predictive models were developed in this study for polyethylene-based 3D micro- and macro-scale metamaterial solutions for thermal radiation control. In this study, the three designs explored for IR camouflaging capabilities are: (1) macro-scale lenticular lens design, (2) macro-scale lenticular lens sandwiched structure, and (3) micro-scale post design. Both the single and sandwiched lenticular lens designs exhibited similar stable emissive trends with high optical light dispersion capabilities, which is efficient for passive camouflage. The micro-scale post design allows highly-customizable solutions to tune the emissivity response of the metamaterials. Actively actuating the post design through strain modulation techniques is a viable option to redshift the emissivity spectrum. Overall, this study (1) aims to guide design decisions for tunable IR emitting surfaces and thermal radiation control using predictive modeling capabilities and (2) demonstrates how practical changes in surface topology result in measurable changes in optical properties.

ACKNOWLEDGMENTS

This research was funded by the Department of National Defence (DND) of Canada program Innovation for Defence Excellence and Security (IDEaS) under Project W7714-228051/001/SV1.herein.

CONFLICT OF INTEREST

The authors declare no conflict of interest.

DATA AVAILABILITY STATEMENT

The data that support the findings of this study are available from the corresponding author upon reasonable request.

REFERENCES

1. A. Butler, C. Argyropoulos, *Appl. Therm. Eng.* **2022**, *211*, 118527.
2. Y. Rao, J. Dai, C. Sui, Y.-T. Lai, Z. Li, H. Fang, X. Li, W. Li, P.-C. Hsu, *ACS Energy Lett.* **2021**, *6*, 3906.
3. A. Kazemi Moridani, R. Zando, W. Xie, I. Howell, J. J. Watkins, J.-H. Lee, *Adv. Opt. Mater.* **2017**, *5*, 1600993.
4. H. R. Seyf, A. Henry, *Energy Environ. Sci.* **2016**, *9*, 2654.
5. B. Fang, S. C. Bodepudi, F. Tian, X. Liu, D. Chang, S. Du, J. Lv, J. Zhong, H. Zhu, H. Hu, et al., *Nat. Commun.* **2020**, *11*, 1.
6. Y. Liu, J. Song, W. Zhao, X. Ren, Q. Cheng, X. Luo, N. X. Fang, R. Hu, *Nanophotonics* **2020**, *9*, 855.
7. L. Li, M. Shi, X. Liu, X. Jin, Y. Cao, Y. Yang, W. Wang, J. Wang, *Adv. Funct. Mater.* **2021**, *31*, 2101381.
8. Q. Kang, D. Li, K. Guo, J. Gao, Z. Guo, *Nanomaterials* **2021**, *11*, 260.
9. L. Long, S. Taylor, X. Ying, L. Wang, *Mater. Today Energy* **2019**, *13*, 214.
10. T. Inoue, M. D. Zoysa, T. Asano, S. Noda, *Nat. Mater.* **2014**, *13*, 928.
11. G. Cai, J. Wang, A. L.-S. Eh, J. Chen, K. Qian, J. Xiong, G. Thangavel, P. S. Lee, *ACS Appl. Mater. Interfaces* **2018**, *10*, 37685.
12. C. Xu, M. Colorado Escobar, A. A. Gorodetsky, *Adv. Mater.* **2020**, *32*, 1905717.
13. P. Chandrasekhar, B. J. Zay, G. C. Birur, S. Rawal, E. A. Pierson, L. Kauder, T. Swanson, *Adv. Funct. Mater.* **2002**, *12*, 95.
14. M. A. Kats, R. Blanchard, S. Zhang, P. Genevet, C. Ko, S. Ramanathan, F. Capasso, *Phys. Rev. X* **2013**, *3*, 041004.
15. S. Dang, H. Ye, *Cell Rep. Phys. Sci.* **2021**, *2*, 100617.
16. N. Lee, J.-S. Lim, I. Chang, D. Lee, H. H. Cho, *ACS Appl. Mater. Interfaces* **2021**, *13*, 43524.
17. N. Lee, T. Kim, J.-S. Lim, I. Chang, H. H. Cho, *ACS Appl. Mater. Interfaces* **2019**, *11*, 21250.
18. T. Shi, Z. Zheng, H. Liu, D. Wu, X. Wang, *Compos. Sci. Technol.* **2022**, *217*, 109127.
19. R. Xu, W. Wang, D. Yu, *Compos. Struct.* **2019**, *212*, 58.
20. A. Choe, J. Yeom, Y. Kwon, Y. Lee, Y.-E. Shin, J. Kim, H. Ko, *Mater. Horiz.* **2020**, *7*, 3258.
21. T. Kim, J.-Y. Bae, N. Lee, H. H. Cho, *Adv. Funct. Mater.* **2019**, *29*, 1807319.
22. T. Han, X. Bai, J. T. Thong, B. Li, C.-W. Qiu, *Adv. Mater.* **2014**, *26*, 1731.
23. H. Zhu, Q. Li, C. Tao, Y. Hong, Z. Xu, W. Shen, S. Kaur, P. Ghosh, M. Qiu, *Nat. Commun.* **2021**, *12*, 1.
24. J. Wang, F. Yang, L. Xu, J. Huang, *Phys. Rev. Appl.* **2020**, *14*, 014008.
25. S. Yang, J. Wang, G. Dai, F. Yang, J. Huang, *Phys. Rep.* **2021**, *908*, 1.
26. J.-P. Huang, *Theoretical Thermotics: Transformation Thermotics and Extended Theories for Thermal Metamaterials*. Springer Nature, Singapore, **2020**.
27. N. Lee, B. Yoon, T. Kim, J.-Y. Bae, J.-S. Lim, I. Chang, H. H. Cho, *ACS Appl. Mater. Interfaces* **2020**, *12*, 8862.
28. H. Kocer, S. Butun, E. Palacios, Z. Liu, S. Tongay, D. Fu, K. Wang, J. Wu, K. Aydin, *Sci. Rep.* **2015**, *5*, 1.
29. S. Walia, C. M. Shah, P. Gutruf, H. Nili, D. R. Chowdhury, W. Withayachumnankul, M. Bhaskaran, S. Sriram, *Appl. Phys. Rev.* **2015**, *2*, 011303.
30. COMSOL Multiphysics® v. 5.6. www.comsol.com. COMSOL AB, Stockholm, Sweden.
31. G. Wu, D. Yu, *Prog. Org. Coat.* **2013**, *76*, 107.
32. J. Yang, X. Zhang, X. Zhang, L. Wang, W. Feng, Q. Li, *Adv. Mater.* **2021**, *33*, 2004754.
33. L. M. Degenstein, D. Sameoto, J. D. Hogan, A. Asad, P. I. Dolez, *Micromachines* **2021**, *12*, 773.
34. I. D. Peggs, B. Schmucker, P. Carey, *Waste Containment and Remediation*, **2005**, pp. 1–16.
35. M. Chen, A. M. Morsy, M. L. Povinelli, *Opt. Express* **2019**, *27*, 21787.
36. RF Module User's Guide. COMSOL Multiphysics® v. 5.6. COMSOL AB, Stockholm, Sweden, **2020**.
37. P.-M. Robitaille, *Progr. Phys.* **2009**, *4*, 3.
38. N. Lee, J.-S. Lim, I. Chang, D. Lee, H. H. Cho, *Int. J. Heat Mass Transfer* **2021**, *173*, 121173.
39. Z. J. Coppens, J. G. Valentine, *Adv. Mater.* **2017**, *29*, 1701275.
40. J. Kim, C. Park, J. W. Hahn, *Adv. Opt. Mater.* **2022**, *10*, 2101930.
41. A. Arya, A. L. Sharma, *J. Mater. Sci. Mater. Electron.* **2018**, *29*, 17903.
42. N. H. Ismail, M. Mustapha, *Polym. Eng. Sci.* **2018**, *58*, E36.
43. J. Mason, S. Smith, D. Wasserman, *Appl. Phys. Lett.* **2011**, *98*, 241105.
44. H. Zhu, Q. Li, C. Zheng, Y. Hong, Z. Xu, H. Wang, W. Shen, S. Kaur, P. Ghosh, M. Qiu, *Light Sci. Appl.* **2020**, *9*, 1.
45. P. Zhao, H. Chen, B. Li, H. Tian, D. Lai, Y. Gao, *Opt. Mater.* **2019**, *94*, 378.
46. C. Y. Zhang, H. F. Cheng, Z. H. Chen, W. W. Zheng, *International Symposium on Photoelectronic Detection and Imaging 2009: Advances in Infrared Imaging and Applications*, SPIE, **2009**, *7383*, 202.
47. K. Gupta, A. Nishkam, N. Kasturiya, *J. Ind. Text.* **2001**, *31*, 27.
48. H. Yu, G. Xu, X. Shen, X. Yan, C. Cheng, *Appl. Surf. Sci.* **2009**, *255*, 6077.
49. H. Jo, J. L. King, K. Blomstrand, K. Sridharan, *Int. J. Heat Mass Transfer* **2017**, *115*, 1065

How to cite this article: H. Pisavadia, A. Asad, D. Sameoto, P. Dolez, J. D. Hogan, *Nano Select*. **2023**, *4,* 263. https://doi.org/10.1002/nano.202200212